Interstadial conditions over the Southern Alps during the early penultimate glacial (MIS 6): a multiproxy record from Rio Martino Cave (Italy)

Eleonora Regattieri [a, b, *], Silvia Querci [c], Giovanni Zanchetta [c, d, e], Elena Zanella [f], Ilaria Isola [b, a], Russell N. Drysdale [g], John C. Hellstrom [h], Federico Magrì [i]

[a] Istituto di Geoscienze e Georisorse, IGG-CNR, Via Moruzzi 1, 56126, Pisa, Italy
[b] Istituto Nazionale di Geofisica e Vulcanologia INGV, Via della Faggiola 32, 56126, Pisa Italy
[c] Dipartimento di Scienze della Terra, University of Pisa, Via S. Maria 53, 56126, Pisa, Italy
[d] CIRSEC Centre for Climatic Change Impact, University of Pisa, Pisa, Italy
[e] Istituto di Geologia Ambientale e Geoingegneria, IGAG-CNR, Via Salaria km29.4, Monterotondo, Rome, Italy
[f] Dipartimento di Scienze della Terra, Università di Torino, Via Valperga Caluso 35, 10125, Torino, Italy
[g] School of Geography, University of Melbourne, Victoria, 3010, Australia
[h] School of Earth Sciences, University of Melbourne, Victoria, 3010 Australia
[i] Associazione Gruppi Speleologici Piemontesi AGSP-Club Alpino Italiano, Torino, Italy

ARTICLE INFO

ABSTRACT

Identifying the hydrological and environmental response of the European Alpine region to different combinations of climate boundary conditions is crucial to advance the reliability of predictive climate models and thus shape climate adaptation policies that will impact millions of people in seven countries. Here we present a high-resolution multiproxy speleothem record (stable oxygen and carbon isotope ratios, petrography and magnetic properties) from Rio Martino Cave (Piedmont, Southern Alps, Italy), which covers the first part of the Penultimate Glacial (early MIS 6, 182−157 ka). During early MIS 6, the combination of high climatic precession and obliquity amplified the peak in Northern Hemisphere (NH) summer insolation intensity at ca. 174 ka to almost interglacial levels, leading to northward migration of the Intertropical Convergence Zone and the enhancement of the boreal monsoon system. At orbital scale, the hydroclimatic record from Rio Martino closely follows the precession pattern, and shows a wet interstadial phase between 180 and 170 ka, peaking at the precession minimum, characterized by glacial retreat and by the likely development of soils and vegetation up to 1900−2000 m a.s.l. in this alpine sector. This phase can be traced across the Southern Alps, and corresponds to pluvial conditions inferred from Western Mediterranean records, and to the interval of deposition of the cold Sapropel S6 in the eastern Mediterranean. We suggest that the interaction between an intensified northwesterly cold flow (relating to increased ice volume under glacial conditions), and the relatively warm waters of the NW Mediterranean (due to the peculiar atmospheric configuration occurring at the precession minimum) strongly enhanced the autumn cyclogenesis in the Northern Tyrrhenian Sea, fuelling intense precipitation to reach the Southern Alps. The Rio Martino record also shows a prominent sub-orbital variability, the overall structure of which is coherent with hemispheric changes in climate driven by cyclic perturbations of North Atlantic conditions related to the operation of the bipolar seesaw.

© 2021 Elsevier Ltd. All rights reserved.

1. Introduction

High-altitude areas like the European Alps are undergoing rapid and profound modifications because of the current climate change (IPCC, 2019). Reliable long-term climate forecasts for the Alps are relevant for large parts of European society, but the complexity of

the Alpine region poses considerable challenges for robust climate modelling. In particular, precipitation changes are less well quantified than temperature changes, and often appear more heterogeneous (Gobiet et al., 2014), translating into uncertainties in climate projections (Suklitsch et al., 2011). Well-dated paleo-proxy records sensitive to changes in regional hydroclimate are useful for addressing issues concerning the underlying mechanisms, timing and pattern of precipitation variability under different climate configurations in the past (Wagner et al., 2019). The study of site-specific proxies can shed light on the local environmental responses, an important issue in the highly vulnerable mountain belt (IPCC, 2019). Here we report a high-resolution multiproxy speleothem record (δ^{13}C; δ^{18}O, growth rate, petrography and magnetic properties) from a flowstone core (RMD7) from Rio Martino Cave (Piedmont, SW Alps, Fig. 1). RMD7 was deposited during the early

part of the penultimate glacial, between ca. 182 and 157 ka, corresponding to the first part of Marine Isotope Stage (MIS) 6 (Margari et al., 2010). During early MIS 6, the combination of high climatic precession and high obliquity amplified the peak in Northern Hemisphere (NH) summer insolation intensity at ca. 174 ka to almost interglacial levels. This forced a northward migration of the Intertropical Convergence Zone (ITCZ), with strong enhancement of NH monsoon systems (e.g. Cheng et al., 2016). The increased monsoon-fed discharge from the Nile River and from (now-fossil) wadi systems in North Africa led to the formation of sapropel layer S6 in the eastern Mediterranean Sea, which is dated to between 165.5 and 178.2 ka based on the speleothem-tuned chronology of Ziegler et al. (2010). Southern Europe and the Mediterranean were thus influenced by two climatic extremes: cold conditions leading to the progressive growth of ice over northern

Fig. 1. Location of Rio Martino Cave (red dot) and other sites mentioned in the text. A: MD-MD01-2444 (Margari et al., 2010, 2014), 977-ODP-977 (Martrat et al., 2007); OH-Ohrid Lake (Wagner et al., 2019), Sanbao Cave (Wang et al., 2008); B: 1- Swiss foreland (Dehnert et al., 2012); 2-Piani Eterni Cave (Columbu et al., 2018); 3- Spannagel Cave (Holzkämper et al., 2005); 4-Azzano Decimo core (Pini et al., 2009); 5-Argentarola Cave (Bard et al., 2002); 6-core PRLG1 (Cortina et al., 2011, 2013, 2015); the pink line is the climatic division of the Alpine Region (after Efthymiadis et al., 2007); C-Simplified geological map of Rio Martino area, the red line is the supposed cave catchment. D-Three-dimensional sketch of Rio Martino Cave showing the sampling locations of RMD7 (this study) and RMD1 (Regattieri et al., 2019a). E– View of Rio Martino catchment, red line as in C, blue lines mark Lateglacial moraine ridges. (For interpretation of the references to colour in this figure legend, the reader is referred to the Web version of this article.)

Europe and enhanced monsoon activity in the NH tropics (Margari et al, 2010, 2014).

An increase in Western Mediterranean precipitation in the autumn-winter season during periods of sapropel formation is widely reported from both paleo-records (Wagner et al., 2019; Regattieri et al., 2015; Toucanne et al., 2015; Milner et al., 2012; Zhornyak et al., 2011; Tzedakis, 2007; Zanchetta et al., 2007) and climate models (Wagner et al., 2019; Bosmans et al., 2015). Specifically, for the early MIS6, wetter and warmer conditions are reported from speleothem and lake records for the eastern Mediterranean (Wagner et al., 2019; Nehme et al., 2018; Roucoux et al., 2011; Vaks et al., 2006; Ayalon et al., 2002), and for the Western Mediterranean and Southern Europe (Isola et al., 2019; Toucanne et al., 2015; Margari et al, 2010, 2014; Wainer et al., 2013; Bard et al., 2002; Plagnes et al., 2002). However, little is known about the corresponding responses in the Alpine region, where records of both orbital and sub-orbital hydro-climate variability are poorly known (Columbu et al., 2018; Pini et al., 2009).

A previous study of a Holocene speleothem from Rio Martino (RMD1) showed that the $\delta^{18}O$ record tracks changes in regional hydrology, whereas the $\delta^{13}C$ and magnetic properties are related to the soil history at the catchment scale (Regattieri et al., 2019a). Using the same approach, here we reconstruct in detail the climatic and environmental conditions at Rio Martino during the first part of MIS 6, and explore their links with glacial history and regional and extra-regional climate. Our aim is to assess the response of this portion of the Alpine region to the peculiar forcing of early MIS 6 climate

2. Site settings

Rio Martino Cave is located at 1530 m a.s.l. in the upper Po River valley (Piedmont, SW Alps, Italy, Fig. 1). The cave characteristics are discussed in previous studies (Regattieri et al., 2019a; Zanella et al., 2018; Magrì et al., 2007) and are only briefly summarized here. The cave has developed within Mesozoic dolomitic carbonates. The catchment area is between 1900 and 2200 m, most of which is characterized by decimetric thick cover consisting of Quaternary glacial and periglacial sediments (Fig. 1). Currently, the catchment hosts a grassland dominated by C3 herbs such as carex (*Carex firma*) and sesleria (*Sesleria albicans*). This vegetation is typical of the Alpine altitude belt (2200−3000 m a.s.l.; Borsato et al., 2015) and its occurrence at lower altitudes of the Rio Martino catchment is related to lowering of the tree-line resulting from long-term anthropic influences. Elsewhere in the Alps, the upper subalpine belt (2200−1900 m a.s.l.), to which the Rio Martino catchment belongs, is characterized by an open conifer forest with dwarf mountain pine (*Pinus mugo*), scattered larix (*Larix decidua*), Swiss stone pine (*Pinus cembra*) and frequent shrubs such as heather (*Calluna vulgaris*) and rhododendron (*Rhododendron ferrugineum*) (Borsato et al., 2015). The cave is crossed by a permanent stream that responds rapidly to meteorological events thanks to direct infiltration where the carbonate body is closer to the surface. Slower water circulation occurs within the glacial sediment, and represents the main source feeding the river and the drip recharge system (Magrì et al., 2007). The mean cave temperature, based on 2 years of monitoring, is 5.3 °C (Magrì et al., 2007). Mean annual precipitation is ca. 1100 mm, with maxima in April−May and October−December. The gridded map of precipitation $\delta^{18}O$ values in Italy (Giustini et al., 2016) indicates values between −12‰ and −10‰ for Rio Martino area. The distribution of long-term mean temperature and precipitation in the Alps is influenced by several large-scale climatic drivers prevailing over the Atlantic, the European continent, and the Mediterranean Basin (Wanner et al., 1997), modulated by local Alpine morphology and topography (Casty et al.,

2005; Frei and Schär, 1998). The single dominant moisture source throughout most of the year for the Southern Alps is the Western Mediterranean (Fig. 1), which contributes up to 35%, with maxima in autumn and minima during winter (Sodemann and Zubler, 2010). During summer, the Mediterranean contribution remains at a fairly high level, and local, convective precipitation increases (ca. 20% of the total from land sources; Sodemann and Zubler, 2010). Precipitation from SE and NE North Atlantic Ocean (Fig. 1) accounts for ca. 23%, and it is mostly confined to the winter months, when a significant negative correlation between the North Atlantic Oscillation (NAO) index and Southern Alpine precipitation is observed (López-Moreno et al., 2011; Efthymiadis et al., 2007; Casty et al., 2005). The NAO index is also positively correlated with temperature, with the correlation becoming stronger at higher altitudes (Lopez-Moreno et al., 2011; Efthymiadis et al., 2007).

3. Methods

3.1. Field sampling and subsampling

RMD7 core was collected from a flowstone located on a lateral branch of the main cave (Fig. 1). The flowstone is embedded between two decimeters-thick sandy units. Dating of the flowstone growing above the upper sandy units yields Late Glacial to Early Holocene (13−9 ka) age (our unpublished data). The RMD7 core is 3.25 cm in diameter and 23 cm long and covers the whole flowstone thickness. It was halved perpendicular to the long axis and one of the polished sections was sub-sampled at 1 mm increments, perpendicular to the growth laminations, using a milling machine with a 1 mm-diameter drilling bit, producing 226 samples for stable C and O isotopes ($\delta^{13}C$ and $\delta^{18}O$) analyses. On the same half, nine prisms of ~150 mg (~5 mm wide along the laminae and 2 mm thick on growth axis) were taken for U/Th dating. The other section was quartered and sliced with a diamagnetic blade of 1 mm producing 48 specimens, 2−4 mm thick, for magnetic analyses. From the other quarter, six partly overlapping thin sections for petrographic analyses were retrieved.

3.2. Microstratigraphic observations

The microstratigraphic features of RMD7 were investigated along the whole core depth by observation of six partly overlapping thin sections with an optical petrographic microscope (Zeiss Laboval 4 ausJena), both in parallel and crossed nicols. Calcite fabrics and petrographic features have been described based on Frisia (2015) and Frisia and Borsato (2010). Several fabric subtypes were recognized and logged along the core depth to create a microstratigraphic log, following Frisia (2015).

3.3. Stable isotope analyses

$\delta^{18}O$ and $\delta^{13}C$ isotope ratios were measured using an Analytical Precision AP2003 continuous-flow isotope-ratio mass spectrometer at the University of Melbourne, Australia, with the method presented in Bajo et al. (2020). Briefly, samples were digested in 105% phosphoric acid for 1 h at 70 °C. Results were normalized using an internal working standard (NEW1, Carrara Marble), calibrated against the international standards NBS18 and NBS19. Results are reported on the VPDB scale. Mean analytical uncertainties are 0.10‰ and 0.05‰ for $\delta^{18}O$ and $\delta^{13}C$, respectively.

3.4. U/Th dating and age modelling

The U/Th dating was performed at the School of Earth Sciences, University of Melbourne, following the method of Hellstrom

(2003). Briefly, samples were dissolved and spiked with a mixed $^{236}U-^{233}U-^{229}Th$ solution. The carbonate matrix was removed with ion-exchange resin, and the purified U and Th fraction diluted in HNO_3 was injected into a multi-collector inductively coupled plasma mass spectrometer (MC-ICPMS, Nu-Instruments Plasma). The $^{230}Th/^{238}U$ and $^{234}U/^{238}U$ activity ratios were calculated using an internally standardised parallel ion-counter procedure and calibrated against the HU-1 secular equilibrium standard. Detrital Th was corrected by applying an empirically derived initial activity ratio ($^{230}Th/^{232}Th)_i$ of 1.3 ± 0.45. This value, and the relative 2σ uncertainty, were calculated following Hellstrom (2006) by using a Monte Carlo procedure based on stratigraphical constraint among the U/Th ages. The applied correction is the same as that employed for the Holocene speleothem RMD1 (Zanella et al., 2018). The age-depth relationship and the resulting speleothem growth rate were calculated using a Bayesian Monte Carlo approach (Drysdale et al., 2005).

3.5. Rock magnetic measurements

Magnetic measurements were performed at the ALP Paleomagnetic Laboratory (Peveragno, Italy) with the methods detailed in Zanella et al. (2018). Briefly, low-field susceptibility (k_m) measurements were performed using a KLY3 kappabridge with a sensitivity of the order of 10^{-8} SI (AGICO). Bulk susceptibility was measured at least five times for each subsample, and the average values and relative standard deviations calculated. Samples were weighed to determine the mass-normalized susceptibility (χ, m^3 kg^{-1}) with the relationship: $\chi = (k/m) \times v$, where m is the mass of the specimen and v the volume, assumed to be 10 cm^3 for each sample. A JR6 (AGICO) spinner magnetometer with a sensitivity of 10^{-6} A/m was used to measure the natural remanent magnetization (NRM, J_r), and the mass-normalized NRM (J) was calculated. Each sample was AF demagnetized (ASC Scientific D-200 demagnetizer) up to peak field of 100 mT, then Isothermal Remanent Magnetization (IRM) curves were obtained by a pulse magnet (Bussi) applying stepwise increasing fields up to 1 T.

4. Results

4.1. Chronology

Nine U/Th ages were obtained from RMD7 (Table 1). One was rejected as an outlier while the remaining eight are in stratigraphic order within the associated age uncertainties and were included in the age-model calculations. The age model spans the interval 182.2 ± 3.9 ka to 156.9 ± 6.1 ka and has a mean associated uncertainty of ~2.8 kyr (Fig. 2). The resulting temporal resolution is, on average, 112 years for the stable isotope record and 549 years for the magnetic record.
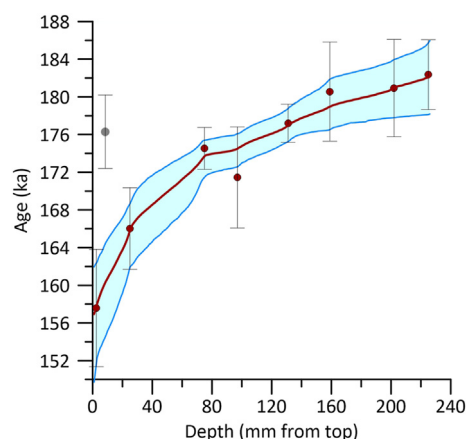

Fig. 2. Age-depth model for RMD7 core, the green shadow represents the 95% uncertainty, in grey the age excluded as outlier. (For interpretation of the references to colour in this figure legend, the reader is referred to the Web version of this article.)

4.2. Microstratigraphy and petrography

RMD7 is composed of light-coloured translucent calcite. It shows darker bands with faint to well-defined laminations (Fig. 3). Microstratigraphic observations reveal that the dominant fabric is columnar elongated (Ce) calcite (Frisia, 2015), a type of speleothem columnar fabric typically observed when the Mg/Ca ratio (molar) in the feed water exceeds 0.3, which is common where the host rock includes dolomite (Frisia, 2015). Columnar fabric and its subtypes are associated with relatively constant drip discharge and low calcite supersaturation state (Frisia, 2015; Frisia and Borsato, 2010). In flowstone RMD7, we observed both compact columnar elongated (Ce), with serrated crystal boundaries and a few lateral overgrowths (Fig. 3.1) and open columnar elongated with lateral overgrowths (CeO$_{lo}$), which is characterized by small elongated pores between crystals partially filled by lateral overgrowths. The CeO$_{lo}$ has been further subdivided into three sub-types on the basis of the density of lateral overgrowths: CeO$_{lo}$-a shows elongated columnar crystals, few elongated cavities and some lateral overgrowths starting from the crystal edges (Fig. 3.3). The amount of detrital material is scarce. In CeO$_{lo}$-c (Figs. 3–6), the detrital content is higher, crystals have irregular edges and are largely covered by lateral overgrowths. Particularly in this sub-type, some of the columnar individuals consist of a mosaic of crystals which seems to indicate small-scale dissolution of lateral overgrowth and syntaxial reprecipitation onto the elongated columnar crystals. This process could be defined as ripening or aggrading neomorphism and is considered to indicate incipient diagenesis (Frisia, 2015). Likely, for RMD7, it is related to the occasional influx of undersaturated waters, such as those from flooding of the cave river during seasonal
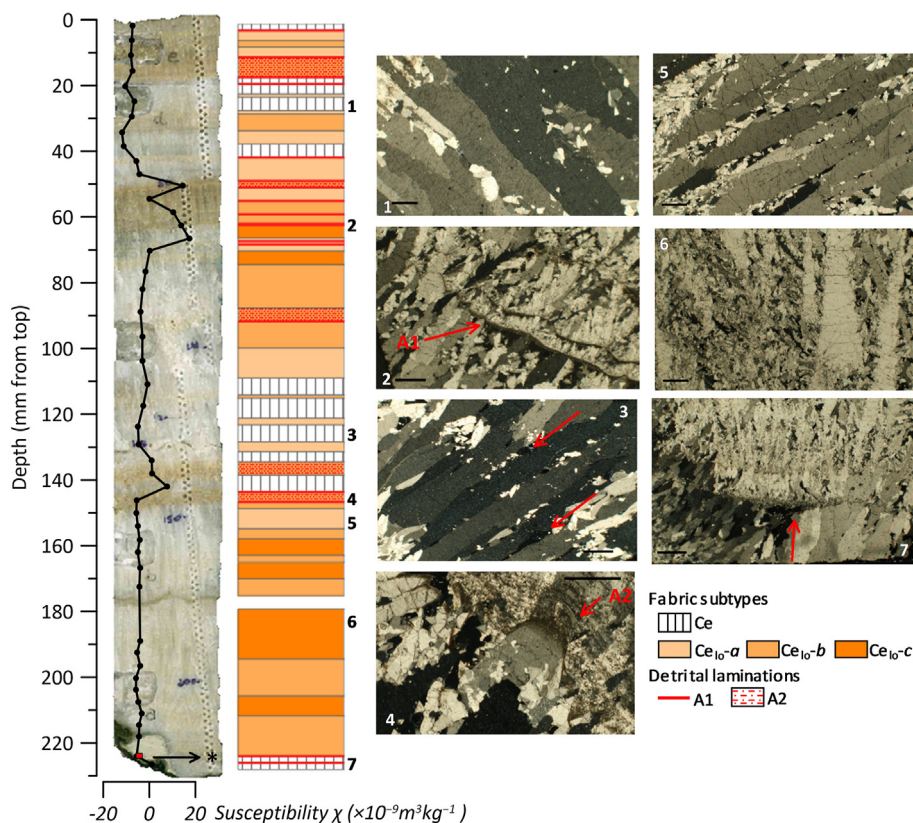
Table 1
Corrected (in bold) and uncorrected U/Th ages for core RMD7. The activity ratios have been standardized to the HU-1 secular equilibrium standard, and ages calculated using decay constants of 9.195 × 10−6 (^{230}Th) and 2.835 × 10−6 (^{234}U). Depths are mm from top. The age in italics was rejected as an outlier.

Sample ID	^{238}U ng/g	Depth (mm)	$^{230}Th/^{238}U$	$^{234}U/^{238}U$	Age uncr (ka)	$^{232}Th/^{238}U$	$^{230}Th/^{232}Th$	Age cr (ka)	2se (ka)
RMD7-2	94	2.5	0.8471	1.0524	173.65	0.113875	7.4	**157.59**	**6.23**
*RMD7-E**	*1.08*	*8.50*	*0.8595*	*1.0485*	*181.96*	*0.041854*	*20.5*	***176.33***	***3.94***
RMD7-D	82	25	0.8498	1.0680	167.86	0.014066	60.4	**166.02**	**4.33**
RMD7-25	88	75	0.8528	1.0555	174.99	0.003565	239.2	**174.53**	**2.22**
RMD7-C	108	97	0.8430	1.0510	172.35	0.006548	128.7	**171.45**	**5.37**
RMD7-131	96	131	0.8595	1.0566	177.81	0.004716	182.3	**177.19**	**2.02**
RMD7-B	83	159	0.8810	1.0666	183.88	0.025597	34.4	**180.56**	**5.27**
RMD7-A		202	0.8786	1.0664	182.74	0.013878	63.3	**180.92**	**5.17**
RMD7-225	28	225	0.8817	1.0575	189.219	0.051407	17.2	**182.36**	**3.71**

Fig. 3. Left: core RMD7 and the sketch of its micropetrographic features, with the mass-susceptibility (χ) plotted in black (the red dot corresponds to sample RMD7-46). On the right, photomicrographs from thin sections. 1-Elongated columnar calcite with sparse lateral overgrowths (Ce); 2-A1 type detrital lamination deposited on Ce_{lo}-b fabrics, lamina indicated by a red arrow; 3-Columnar calcite with lateral overgrowths (Ce_{lo}-a) and elongated pores (marked by arrows); 4-A2 type detrital lamina (marked with red arrow), deposited over an A1 lamination; 5- Fabric Ce_{lo}-b on the left passing to Ce_{lo}-a on the right; 6- Ce_{lo}-c showing elongated columnar crystals with abundant lateral overgrowths and high detrital content. 7-Silty detrital lamina at the base of RMD7 (marked by a red arrow). The black bars on the photomicrographs are 1 mm. (For interpretation of the references to colour in this figure legend, the reader is referred to the Web version of this article.)

melting, over the flowstone surface. Importantly, due to its episodic nature, the spatial and temporal scale of this diagenetic modification is much shorter than the temporal resolution of the record, and thus has negligible consequences on the preservation of the original geochemical signals. CeO_{lo}-b shows features intermediate between CeO_{lo}-a and CeO_{lo}-c (Fig. 3.5). The transition between the different subtypes is usually gradual. The alternation of compact and open-columnar fabric in different portions of the same speleothem commonly indicates a change in drip (flow) rate (Frisia and Borsato, 2010), with the CeO forming from a thicker water film under higher drip rate and with low degassing rates (Frisia, 2015). The detrital phase of RMD7 is mostly composed of cryptocrystalline and opaque, dark material, comprising clay minerals, soil colloids and iron oxides. It occurs both as diffuse material and in thin laminations parallel to the flowstone surface. Two types of lamination can be identified: A1 and A2. A1 laminations are more marked and continuous (Fig. 3.2). Their presence is associated with partial erosional features, where crystals show irregular (rounded or jagged) apical terminations. These erosional surfaces do not represent true hiati, as some crystals show continuous growth through the lamina. A2 laminations are not associated with erosion features, and are thinner and often discontinuous (Fig. 3.4). In addition to A1 and A2 lamina, a 1 mm-thick silty layer occurs close to the core base (227 mm from top: Fig. 3.7)

4.3. Magnetic properties

Rock magnetic measurements are reported in Table S1. Bulk susceptibility of RMD7 (k_m) ranges from −1.5 μSI to 2.08 μSI and its mass magnetic susceptibility (χ) between and -11.88×10^{-9} m^{3}kg^{-1} and 14.5×10^{-9} m^{3}kg^{-1} (Fig. 4), with only one sample showing χ of 123.82×10^{-9} m^{3}kg^{-1}. Most of the samples have small negative magnetic susceptibilities. Calcite mass susceptibility is about -4.46×10^{-9} m^{3}kg^{-1} (Almqvist et al., 2010), thus most of the χ series of RMD7 reflects the prevailing contribution of diamagnetic calcite. χ values lower than the reference value can be explained by the fact that speleothems consist of crystal aggregates, where each crystal may have its c-axis that is not perfectly parallel to those of the adjacent individuals (Zhu et al., 2012; Borradaile and Henry, 1997). χ values $> -4 \times 10^{-9}$ m^{3}kg^{-1} are due to the input of paramagnetic and ferromagnetic detrital material, sourced from the bedrock, the regolith and the soil (Zanella et al., 2018). Positive values are only distributed in three sections of RMD7 core, at 181.6 ± 3.4 ka (sample RMD7-46, 123.8×10^{-9} m^3 kg^{-1}, corresponding to the silty layer identified in thin section), between 177.4 ± 1.8 and 176.4 ± 1.7 ka and between 173.9 ± 1.8 and 170.3 ± 3.2 ka (Fig. 4). These intervals correspond to darker bands, A1 type laminations and to CeO_{lo}-b and and CeO_{lo}-c fabric subtypes (Figs. 3 and 4). The mass-normalized natural magnetization intensity (J) varies between 0.28×10^{-5} Am^2 kg^{-1} and 39.24×10^{-5} Am^2 kg^{-1}, with an average value of $4.50 \cdot 10^{-5}$ Am^2 kg^{-1} (Fig. 4). The J and the χ series are significantly correlated (r = 0.63, excluding RMD7-46). The correlation increases (r = 0.66) when only the values higher than the calcite background (-4×10^{-9} m^{3}kg^{-1}) are considered, and is not significant at more negative χ values (r = 0.04) (Fig. S1). This indicates that both J and χ spikes are
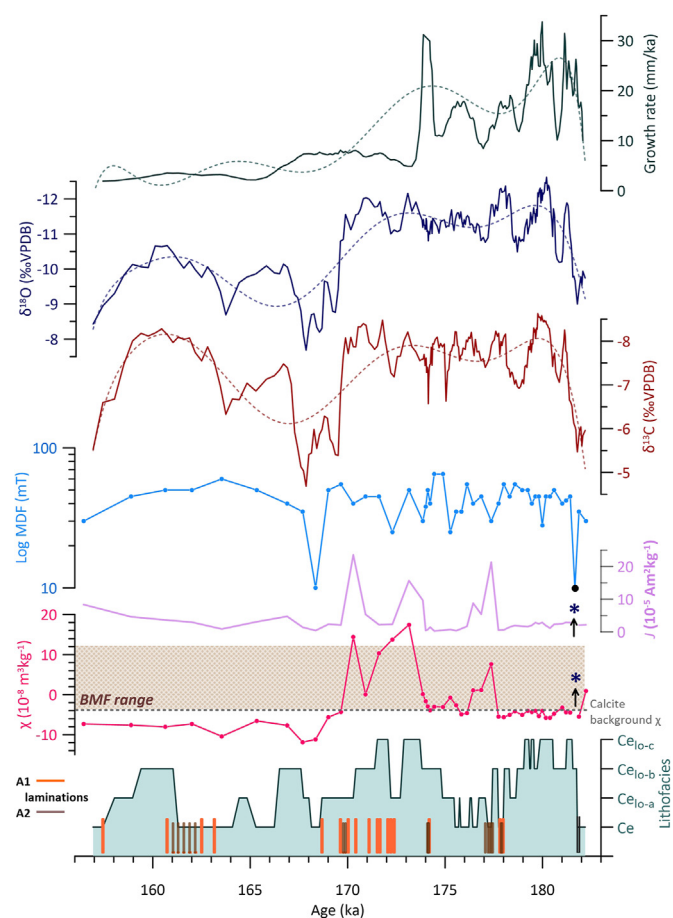
Fig. 4. Results vs age for RMD7 core. From bottom: micropetrographic log and detrital laminations; mass-normalized magnetic susceptibility (χ; 10^{-8} m^{3}kg^{-1}), the dotted grey line is the bulk calcite χ value, the brown-shaded rectangles indicate the range of χ values defining the background magnetic flux (BMF, Regattieri et al., 2019). Sample RMD7-46 is not reported on the χ plot and its position is marked by an asterisk. Natural Remanent Magnetization (J; 10^{-5} Am^{2}kg^{-1}); Median Destructive Field (MDF, mT, on a logarithmic scale, sample RMD7-46 reported in black); δ^{18}O (‰ VPDB); δ^{13}C (‰ VPDB); 3 points-smoothed growth rate (mm/kyr), dashed lines are 10th order polynomial fits showing the long term trend of the time series. (For interpretation of the references to colour in this figure legend, the reader is referred to the Web version of this article.)
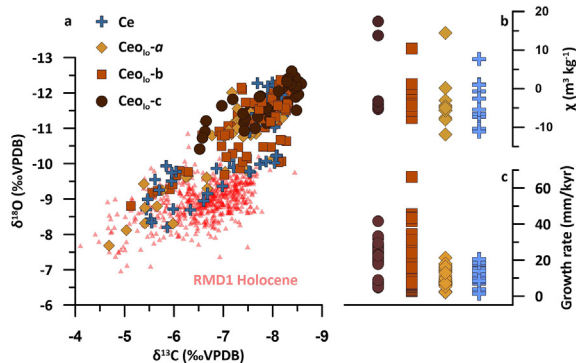

Fig. 5. left: Correlation between stable C and O isotopes by fabric subtype. Data from Holocene speleothem RMD1 (light red triangles) are also shown (Regattieri et al., 2019a); right: Susceptibility values and growth rate for the different fabric subtypes. Ce = elongated columnar; Ce$_{lo}$ = elongated columnar with lateral overgrowth (following Frisia (2015); see section 4.2 for details). (For interpretation of the references to colour in this figure legend, the reader is referred to the Web version of this article.)

essentially controlled by changes in the concentration of para-magnetic or ferromagnetic detrital minerals.

The Median Destructive Field (MDF) obtained by the AF demagnetization curves, and defined as the magnetic field required to reduce the magnetic intensity by half, characterizes the stability of the carriers of remanent magnetization, and is considered a proxy for the magnetic grain populations in the speleothem sample. Typically, increasing/decreasing MDF would suggest a decrease/increase in the average grain size (Bourne et al., 2015). MDF values of RMD7 range from 65 to 10 mT, with an average value of 43 mT (Fig. 4). The MDF shows a negative correlation with χ and J (r = −0.42 and −0.40, respectively, Fig. S1). For samples with susceptibility > -4 × 10^{-9} m^{3}kg^{-1}, the average is slightly lower (40 mT) and r = −0.52. This suggests that the magnetic minerals responsible for the susceptibility spikes are also characterized by a coarser grain size, adding support to their detrital origin. This is particularly evident for sample RMD-46, which shows the highest susceptibility (up to 124 × 10^{-9} m^{3}kg^{-1}) and the lowest MDF (10 mT), suggesting the presence of magnetic mineral particles in the multidomain (MD) size range (Fig. S1) (Bourne et al., 2015). On the other hand, when only samples with χ < −4 × 10^{-9} m^{3}kg^{-1} are considered, the correlation between χ and MDF becomes positive, with r = +0.40, and the average increases to 45 mT, suggesting finer and more uniform magnetic grain size.

4.4. Stable isotopes and growth rate

δ^{13}C, δ^{18}O and growth rate time-series of RMD7 are shown in Fig. 4 and reported in Table S2. The stable isotope ratios range from −12.62‰ and −7.68‰ for carbon and from −8.62‰ to −4.69‰ for oxygen. The two isotope series show a significant statistical correlation ($r^2 = 0.69$) and a very similar pattern (Fig. 4). The common long-term trend shows a rapid decrease of isotope values in the first two millennia of growth, then an interval comprising the most negative values between ca. 180 and 170 ka. Between ca. 170 and 167 ka they show an abrupt interval of increasing isotope ratios (up to 3‰ of variation for both series) and reach the less negative values of the whole record at 167.8 ± 3.6 ka. After this, both ratios decrease rapidly, with the δ^{13}C showing values comparable with that of the first interval but the δ^{18}O values remaining 1.5−2‰ higher. In the last few millennia of growth, from ca. 160 to 157 ka, both series rapidly increase up to the end of the record. Superimposed on the long-term variations, is significant millennial-scale variability coherently expressed by both isotope records and particularly pronounced in the first interval up to ca. 170 ka (Fig. 4). Growth rate varies between 50 and 3 mm/kyr and shows a major decrease at ca. 176 ka. The long-term growth-rate trend to some extent mimics that of the stable isotopes ratios (Fig. 4), especially in the first interval up to 170 ka.

5. Discussion

5.1. Significance of RMD7 deposition and insights into soil conditions

In Alpine caves, the occurrence of speleothem deposition itself provides information on climate conditions (e.g. Holzkämper et al., 2005). RMD7 deposition indicates cave air temperatures >0 °C and a precipitation/evaporation ratio (P/E) > 1 between ca. 182 and 157 ka. Speleothem growth during glacial intervals in alpine caves has been related to climate-induced switches from a cold-to a warm-based glacier above the cave (Hauselmann et al., 2015; Luetscher et al., 2011; Holzkämper et al., 2005; Spötl et al., 2004; Spötl and Mangini, 2007). A warm-based glacier maintains the cave temperature above 0 °C and provides a drip-water supply when mean
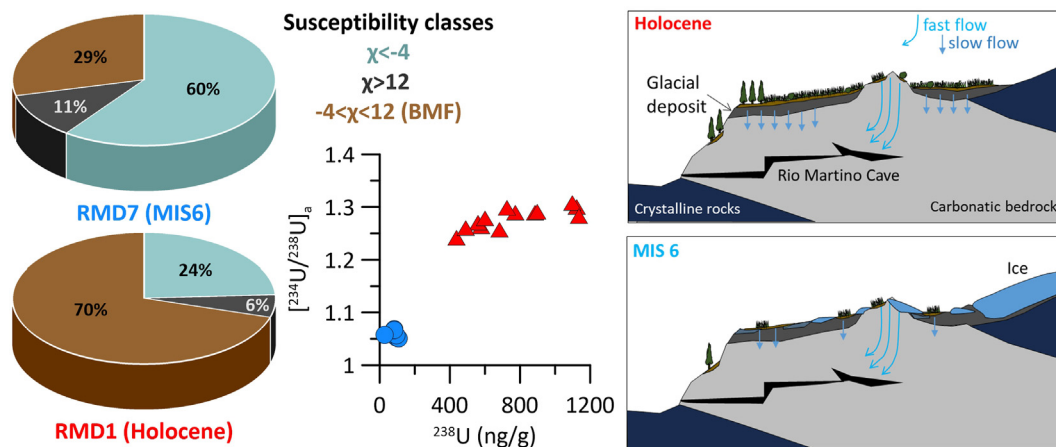
Fig. 6. Left panel- Comparison between susceptibility values for RMD7 (MIS6, this study) and RMD1 (Holocene, Regattieri et al., 2019). Susceptibility (χ) expressed in 10^{-8} m³kg⁻¹. Central panel [²³⁴U/²³⁸U] plotted vs. ²³⁸U concentration for RMD1 (blue dots, Holocene) and RMD7 (red triangles); right-Sketch of proposed catchment and soil settings for the Holocene and the MIS6. (For interpretation of the references to colour in this figure legend, the reader is referred to the Web version of this article.)

annual air temperature at the surface is below freezing (Paterson, 1994). However, records from these caves usually show positive $\delta^{13}C$ values, indicating ^{13}C-enrichment from the bedrock, enhanced by pyrite oxidation, and a lack of ^{13}C-depleted soil derived CO_2 (Luetscher et al., 2011; Spötl and Mangini, 2007; Holzkämper et al., 2005; Spötl et al., 2004). RMD7 has average $\delta^{13}C$ values of $-7.5‰$ (Fig. 4). Assuming a simplified system working near isotopic equilibrium at each stage, it is possible to obtain a raw estimation of the $\delta^{13}C$ of a labile soil carbon pool in equilibrium with the speleothem calcite (Bajo et al., 2017; Regattieri et al., 2014; Rudzka et al., 2011). Considering ca. 1‰ of fractionation between $CaCO_3$ and HCO_3^- (Romanek et al., 1992), RMD7 calcite would have precipitated from a seepage water having a dissolved inorganic carbon $\delta^{13}C_{DIC}$ of -8.5‰. Assuming "open system" conditions (i.e. isotopic equilibrium maintained between the DIC and the coexisting isotopically soil CO_2, implying that the speleothem retains a strong imprint of the biogenic $\delta^{13}C$, with no detectable contribution from the carbonate host rock; Bajo et al., 2017; Hendy, 1971), and a HCO_3^- and $CO_2(g)$ fractionation of 9.0‰ (Zhang et al., 1995), the resulting theoretical $\delta^{13}C$ value of soil CO_2 is -18.5‰. The $\delta^{13}C$ of soil CO_2 can be assumed to be close to that of the $\delta^{13}C$ of soil litter, considering a fractionation of 4.4‰ caused by different diffusion coefficients for $^{12}CO_2$ and $^{13}CO_2$ (Cerling et al., 1991). This results in a calculated value of $-23‰$ for a soil CO_2 in equilibrium with RMD7 calcite. The $\delta^{13}C$ of soil CO_2 depends largely on climate-driven changes in vegetation type (e.g. C3 vs. C4 plants) and vegetation density (e.g. Genty et al., 2001). A significant proportion of C4 vegetation (average $\delta^{13}C$ value of soil CO_2 -17‰, Ehleringer et al., 2000) is not reported in the central-western Mediterranean during the Quaternary period, particularly for the Alps (Borsato et al., 2015). Soil $\delta^{13}C$ at C3 vegetation sites is expected to be in the range -26 to $-20‰$ (Rudzka et al., 2011; Cerling and Quade, 1993), thus the value calculated from RMD7 calcite strongly suggests a prevalent input of CO_2 from soil biological activity under a prevalent C3 vegetation. Deviations from this simple model are likely to occur during actual speleothem deposition. Complete isotopic equilibration may not occur between soil CO_2 and the DIC, with deviations toward "closed system" behaviour and a more pronounced contribution of ^{13}C-enriched CO_2 from bedrock dissolution (Bajo et al., 2017; Rudzka et al., 2011; Hendy et al., 1971). Furthermore, DIC isotopic composition may evolve after equilibration due to the different contributions of bedrock dissolution and/or prior calcite precipitation (PCP, Fairchild and Treble, 2009). Finally, lowering of

drip rates and/or stronger cave ventilation, promoting preferential degassing of $^{12}CO_2$, can further affect the final speleothem $\delta^{13}C$ (Tremaine et al., 2011). However, it must be noted that each of the abovementioned factors tends to drive the $\delta^{13}C$ toward higher values, implying an even "lighter" initial CO_2 flux (Rudzka et al., 2011; Tremaine et al., 2011). An alternative hypothesis to explain the low carbon isotope ratios of RMD7 is that 'light' CO_2 evolved from the respiration of microbial communities that are known to dwell at the interface between ice and rock in wet-based glaciers. In this hypothesis, a warm-based glacier would have covered the catchment. Subglacial microbial communities scavenge ^{13}C-depleted carbon from buried/fossil soil, inherited from the preceding interglacial, and/or use chemolitothrophic pathways that source energy from minerals in the rock or use dead organic carbon (Frisia et al., 2017; Boyd et al., 2014). The CO_2 evolved by microbial respiration would be analogous to that evolved in soil, and indeed $\delta^{13}C$ values between $-11‰$ and $-9‰$ have been reported for subglacial carbonate crusts developed on non-karstic rocks (Refsnider et al., 2014; Thomazo et al., 2017). Columnar calcite formed in the Holocene in the Milchbach cave, under the Upper Grindenwald Glacier (Switzerland), have $\delta^{13}C$ values as low as $-3‰$ (Luetscher et al., 2011). Similarly, Sieben Hegste stalagmites formed during the Last Glacial Maximum under an ice-covered catchment have columnar calcite fabric, but $\delta^{13}C$ values that are positive, as the cave system is large and affected by ventilation (Luetscher et al., 2015). Thus, based on existing data from speleothems formed in the European Alps under wet-based glaciers, the RMD7 $\delta^{13}C$ values are more consistent with CO_2 sourced from soil. Moreover, it is noteworthy that both the macroscopic and microscopic appearance of RMD7 are very similar to the Holocene flowstone RMD1, and both show a similar range of $\delta^{13}C$ and $\delta^{18}O$ values (Fig. 5). These considerations strongly suggest that at least part of the Rio Martino catchment was ice-free during the growth period of RMD7, and that climate conditions allowed the development of soils and vegetation.

The comparison between RMD7 and the Holocene speleothem RMD1 (Regattieri et al., 2019a) raises a further hypothesis about soil status during MIS 6. For RMD1, susceptibility values $-4 < \chi < 12 \times 10^{-8}$ (m³kg⁻¹) have been interpreted as representative of changes in the concentration of fine-grained material deposited via diffuse infiltration through the host rock. This "background magnetic flux" (BMF) mostly derives from pedogenic magnetite and is delivered to the speleothem due to soil erosion and water

infiltration. The cause of higher BMF background values in the early Holocene have been attributed to a steady flux of material from a well-developed soil. Conversely, a more "spiked" behaviour during the late Holocene was related to reduced vegetation and enhanced soil erosion. The comparison between RMD1 and RMD7 (Fig. 6) shows a much lower percentage of samples in the BMF range for RMD7 (29% vs 70%). The formation of magnetite is favoured in well-drained, well-developed soils (Maher et al., 2003). The reduced BMF in RMD7 may thus indicate the presence of less-evolved or poorly drained soil in MIS6 compared to the Holocene. Further insights can be inferred by comparing the initial $^{234}U/^{238}U$ activity ratios- $[^{234}U/^{238}U]_i$ - measured for the dated samples of both speleothems (Fig. 6). U isotopes do not fractionate during calcite deposition, thus the speleothem $[^{234}U/^{238}U]_i$ reflects that of the solution from which they formed (e.g. Hellstrom and McCulloch, 2000). Variations in speleothem $[^{234}U/^{238}U]_i$ have been related to changes in the relative proportion of U derived from carbonate bedrock versus that originating in soil (Hercman et al., 2020; Frumkin and Stein, 2004; Ayalon et al., 1999; Kaufman et al., 1998). Water interacting with thicker and more developed soil exhibits a higher ^{234}U content due to greater mineral-water interaction times and to leaching of organic and inorganic colloids preferentially transporting ^{234}U (Riotte et al., 2003). Further, longer water residence times may allow a greater proportion of direct ^{234}U recoil in water, resulting in elevated U isotope ratios during periods of slower flow (Hellstrom and McCulloch, 2000). $[^{234}U/^{238}U]_i$ of both Rio Martino speleothems is > 1, but it is systematically higher for the Holocene flowstone (average 1.28 vs 1.06), which also shows higher ^{238}U concentration (768 vs 83 ng/g), Fig. 5. The lower $[^{234}U/^{238}U]_i$ may thus suggest a reduced soil-water interaction for the MIS6 sample, possibly due to a thinner, coarser or discontinuous soil cover and/or to faster infiltration. Also, microstratigraphic analyses show that RMD1 is composed predominantly of compact Ce calcite, suggesting relatively slow and constant drip rates (Regattieri et al., 2019a), whereas RMD7 shows the alternation of Ceo_{lo} fabric subtypes, suggesting higher flux and a more variable discharge, especially in the ca. 180−170 ka period (Fig. 4). In RMD7, the more disturbed CeO_{lo}-b and CeO_{lo}-c fabrics also show slightly higher magnetic susceptibility and growth rate, and a more variable MDF (Fig. 5). This suggests a more irregular hydrological regime with respect to the Holocene, with enhanced infiltration and increased coarser detrital transport, likely arising from episodic flooding of the cave during the melting season, especially in the 180−170 ka interval (Fig. 4). It must be taken into account that RMD7 and RMD1 come from two different, though adjacent, cave galleries (Fig. 1), thus the observed differences in magnetic, geochemical and lithological properties may simply be due to separate drips feeding systems, interacting with different lithologies and/or characterized by diverse residence times. However, the comparison of the different proxies consistently points to reduced soil development during the MIS 6 compared to the Holocene, and shows evidence for a higher discharge variability.

5.2. The hydrological significance of the $\delta^{18}O$ record

The calcite $\delta^{18}O$ is the most commonly used paleoclimate proxy from speleothems (e.g. Lachniet, 2009). The main underlying assumptions to its use are that: i) calcite precipitation occurs close to isotopic equilibrium; and ii) the $\delta^{18}O$ of the drip water reflects the $\delta^{18}O$ of the precipitation. Deposition at equilibrium in calcite speleothems is probably rare (Daëron et al., 2019). Recent literature suggests that there are many possible pathways of calcite crystallization. These include particle-mediated nucleation and/or transformation from a microbial-mediated, amorphous, metastable carbonate phase (Frisia et al., 2018; Demeny et al., 2016). The

diverse pathways may influence the preservation of original chemical and physical properties of the forming fluid, and often result in apparent age inversions due to U mobilization (Frisia et al., 2018). Typically, bio-mediated speleothem calcite is characterized by mosaic or micritic fabrics (Frisia et al., 2018; Luetscher et al., 2011). The stratigraphic coherence among U/Th ages and the columnar fabrics observed in RMD7 suggest inorganic deposition occurring in quasi-equilibrium condition (Frisia and Borsato, 2010), and the absence of significant diagenesis. Although the open-columnar fabric is related to increasing degree of disequilibrium, and the presence of lateral overgrowth may be indicative of incipient diagenesis, stable isotope values for the different fabric sub-types identified along RMD7 largely overlap (Fig. 5). Furthermore, the isotope time series do not exhibit important and abrupt shifts related to microstratigraphic changes, suggesting the absence of large kinetic isotope fractionation or diagenetic offsets among the fabric sub-types (Fig. 4).

A recent global compilation of cave water/precipitation monitoring data shows that the drip water $\delta^{18}O$ is most similar to the amount-weighted precipitation $\delta^{18}O$ when mean annual temperature is < 10 °C (Baker et al., 2019), as in the case of Rio Martino Cave. Thus, we can assume that the $\delta^{18}O$ values of RMD7 reflect that of the meteoric precipitation occurring during its formation. The $\delta^{18}O$ composition of RMD1 has been interpreted as related to hydrological variations, with lower and higher values indicating wetter and drier periods, respectively (Regattieri et al., 2019a). This interpretation is commonly applied to Mediterranean speleothems (Regattieri et al, 2018, 2019b; Tzedakis et al., 2018; Columbu et al, 2017, 2018; Finné et al., 2014; Bar-Matthews et al., 2003; Bard et al., 2002) and to southern Alpine speleothems (Columbu et al., 2018; Belli et al., 2013). It relies on the observation, made by Bard et al. (2002), that the $\delta^{18}O$ of western-central Mediterranean precipitation is strongly influenced by variation in the amount of rainfall (with a gradient of ca. −2‰ per 100 mm/month). Instead, temperature variations cause only a small fractionation in Mediterranean meteoric precipitation (ca. +0.3‰/°C), which is counterbalanced by the temperature-dependent fractionation occurring at the site of calcite deposition (ca. −0.2‰/°C, Kim and O'Neil, 1997, i.e. similar in magnitude, but opposite in sign). On the contrary, northern Alpine and central Europe speleothem $\delta^{18}O$ series are usually interpreted as being positively related to temperature variations (e.g. Häuselmann et al., 2015; Spötl and Mangini, 2002). This is because of the stronger temperature-dependence of fractionation affecting meteoric precipitation in those regions (ca. +0.58‰/ °C; Rozanski et al., 1993) and to the negligible influence of the "amount effect" on the isotopic composition of precipitation. Additional influences on the $\delta^{18}O$ can be exerted by changes in the seasonality of the precipitation. Winter and summer precipitation are ^{18}O-depleted and ^{18}O-enriched, respectively, thus a bias toward one season of recharge could affect the $\delta^{18}O$ signal recorded in the calcite. In particular, water derived from ice and snow melt usually shows depleted values. Noteworthy in RMD7, the fabric subtypes, CeO_{lo}-b and CeO_{lo}-c, indicate the highest flux variability, and correspond to lower $\delta^{18}O$ values (Fig. 6) They are also, on average, more negative than the Holocene sample RMD1 (Fig. 6). This possibly reflects a stronger influence of seasonal snow and ice melt on the annual budget. Changes in the location (Luetscher et al., 2015), or in the isotopic composition of the source of precipitation, can be also reflected in the speleothem $\delta^{18}O$ (Marino et al., 2015; Bajo et al., 2020.

5.3. The RMD7 record in the alpine context

Based on the proxy interpretation presented above, the multi-proxy record from RMD7 shows the wettest conditions, the highest

hydrological instability at the millennial scale, and possibly enhanced influence of seasonal infiltration of meltwater, in the 180−170 ka period. From 170 ka, and especially between 170 and 163 ka, the reduced growth rate and the higher stable isotope ratios suggest colder and drier conditions. This interval is followed by a partial recovery and by a further deterioration after 160 ka, with possibly reduced seasonal melting due to reduced ablation and/or perennial snowpack, permafrost or glaciers developing in the catchment and leading to the end of deposition at 158 ka. To place the period of RMD7 growth in the general frame of Alpine glaciation is challenging because the timing and extension of the penultimate glaciation over the Alps is poorly constrained. The few available direct and chronologically constrained lines of evidence (U/Th dating on cement, luminescence and exposure dating of erratic boulders and glacio-fluvial deposits) suggest that a very prominent glaciation, much larger than the LGM, occurred in the Swiss and German sectors of the Alps sometime between 170 ka and 140 ka, and may represent the most extensive glaciation (MEG) for the area (Dehnert et al., 2010; Graf et al., 2007). Particularly, in the Swiss Alpine foreland (Fig. 1), it has been subdivided into two separate ice advances, the most extensive at ca. 185 ka, followed by retreat after 180 ka and by minor re-advances during the period 150−140 ka (Dehnert et al., 2012). No direct glacial evidence is available to our knowledge for the Rio Martino area, but the RMD7 growth interval is consistent with the phase of glacier regression in the Swiss record between 180 and 150 ka (Denhert et al., 2012). For the last glaciation, geomorphological and geochronological investigations from the Gesso Valley, a similar environment located in close proximity to Rio Martino, suggest that glaciers extended to 1000 m a.s.l at ca. 16−17 ka, and report an age of 13 ka for glacial deposits located at 1800 m a.s.l (Federici et al., 2017 and references therein). The extensive moraine ridges that can be easily identified in the current topography above Rio Martino are located at a similar altitude (Fig. 1). Therefore they can be reasonably assigned to the same phase, suggesting a near-fully glaciated catchment at that time (Fig. 1). This suggests a smaller ice cover during the 183−157 ka period compared to 13 ka, and places limits on ice extent during this interstadial phase.

Further constraints on the timing and magnitude of the penultimate glaciation can be indirectly inferred from others Alpine speleothem records. Between ca. 192 and 137 ka, speleothem deposition ceased at Spannagel Cave (2400 m a.s.l., Austrian Alps, Figs. 1 and 7; Hölzkamper et al., 2005), suggesting that glacial conditions were maintained at altitudes higher than Rio Martino, at least on the northern side of the Alps. In the Piani Eterni karst system (Fig. 1, Italian Alps, 1800 m a.s.l; Columbu et al., 2018), phases of speleothem deposition match transitional climate periods of the last 375 ka. Growth is inhibited during most glacial peaks because of cold and dry conditions, whereas during full interglacials, the generally wetter climate and the melting of higher-altitude glaciers cause flooding of the ephipreatic levels, causing cessation of deposition (Columbu et al., 2018). During the MIS7a-MIS 6 interval, the Piani Eterni record shows an interval of growth between 195.2 and 182.1 ka (MIS 7 to MIS6 transition), followed by a hiatus until 169.2 ka (Fig. 7). This hiatus corresponds precisely with the wettest and most hydrologically unstable interval inferred from the RMD7 record (Fig. 7), supporting the notion of a flooding phase at Piani Eterni. Interestingly, an interval of cool-temperate forest expansion was identified in the pollen record from the Azzano Decimo plain, located between the Adriatic coast and the SE alpine foreland (Pini et al., 2009, Fig. 1). This interval postdates the marine regression at the end of MIS 7a and precedes the onset of fluvioglacial deposition related to the growth of the upstream Tagliamento glacier, whose maximum expansion for the MIS 6 was likely attained at ca. 150 ka (Pini et al., 2009). Thus, the post-MIS 7
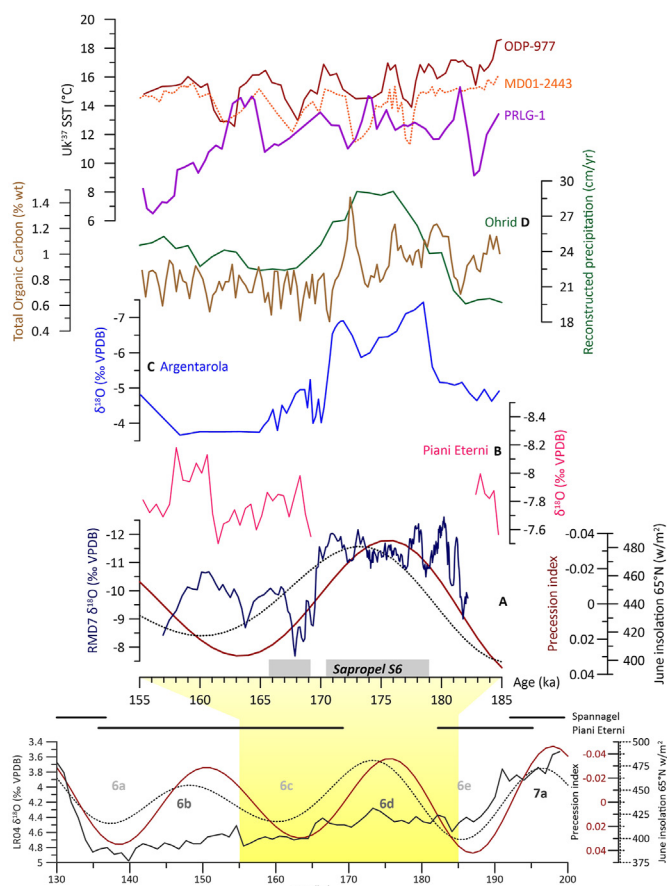

Fig. 7. Upper panel: A) the RMD7 δ18O record (in blue, this study) with superimposed the summer insolation intensity at 65°N (dotted line) and the precession index (red line); B, The δ18O record from Piani Eterni Cave (Columbu et al., 2018); C) the δ18O record from Argentarola Cave (Bard et al., 2002); D) Lake Ohrid modelled precipitation (green, Wagner et al., 2019) and Total Organic Carbon (TOC) content (brown, Francke et al., 2016). E) Alkenone SST records from marine cores PRLG-1 (purple, Gulf of Lyon, Cortina et al., 2015), core MD01-2444 (dotted orange, Iberian Margin, Martrat et al. ref) and core ODP-977 (brown, Alboran sea, Martrat et al., 2007). The timing of deposition of Sapropel S6 (following the chronology of Ziegler et al., 2010) is also shown. Lower panel: interval of speleothem deposition from Spannagel (Holzkämper et al., 2005) and Piani Eterni caves (Columbu et al., 2018) and orbital parameters (June insolation intensity at 65°N and precession index, Laskar et al., 2009). The global benthic stack LR04 (Lisiecki and Raymo, 2005) is also shown as reference. (For interpretation of the references to colour in this figure legend, the reader is referred to the Web version of this article.)

forest expansion at Azzano may be coincident with the wettest period between 180 and 170 ka, whereas the ensuing interval of forest contraction, progressively leading to steppe vegetation, may be coincident with the deterioration trend observed in the speleothems since 170 ka. Overall, the presented evidence points to a wetter and warmer early MIS 6 interstadial phase, promoting glacier retreat and soil and vegetation development over the southern Alps, followed by a trend towards drier and colder conditions during the late MIS 6.

5.4. Mediterranean influence over the Southern Alps at time of sapropel S6 deposition and influence of boundary conditions

The Alpine interstadial inferred from the Rio Martino record matches closely, both for timing and magnitude of the δ18O shift, the stalagmite record from Argentarola Cave (Figs. 1 and 7; Southern Tuscany, Bard et al., 2002), and the pattern precisely follows that of the precession index (Fig. 7). At Argentarola, the δ18O

depletion over this period has been primarily related to the amount effect, and interpreted as a prominent humid period over the western Mediterranean, coincident with deposition of Sapropel S6 in the eastern Mediterranean. The atmospheric configuration related to sapropel formation (i.e. the northward migration of the ITCZ during high climatic precession) amplified subsidence over, and persistence of, summer high-pressure systems in the Mediterranean, leading to warmer and drier summers and higher sea-surface temperatures (Wagner et al., 2019). This leads to amplification of local cyclogenesis, causing intense autumn precipitation in the northern Mediterranean borderlands, as recently shown at Lake Ohrid for interglacial sapropels of the last 1.3 Ma (Fig. 1; Southern Balkans, Wagner et al., 2019). The timing of the increase in western Mediterranean precipitation apparent from Argentarola and Rio Martino corresponds to an increase in the Total Organic Carbon (TOC) content in the Lake Ohrid sediment (Fig. 7), a proxy for lake primary productivity influenced by temperature and precipitation (Francke et al., 2016). It is also consistent with Ohrid modelled precipitation over the same period (Fig. 7). This coherency extends the mechanism to the cold sapropel S6, and suggests that the effect of enhanced local cyclogenesis for this interval was not restricted to the Mediterranean, but also reached the Southern Alps

It is noteworthy that the Holocene record from Rio Martino does not show prominent changes during the deposition of Sapropel S1 (Regattieri et al., 2019a), whereas wetter conditions are inferred from central Italy (Tuscany) speleothems between 8.9 and 7.3 ka (Zhornyak et al., 2011; Zanchetta et al., 2007). Over this period, a compilation of Alpine records shows an enhanced eastward penetration of Mediterranean precipitation, as expected, but also cooler and wetter summer conditions, possibly leading to a small glacial expansion (Spötl et al., 2010 and references therein). This difference between the Alpine response during the intervals of deposition of S1 and S6 may be due to the peculiar combination of the MIS6 boundary conditions. During glacial periods, the increased size of boreal ice sheets caused a southward shift of subpolar low-pressure systems, and a more sub-zonal atmospheric circulation compared to the Mid-Holocene (Luetscher et al., 2015; Pausata et al, 2009, 2011; Kuhlemann et al., 2008). This atmospheric configuration led to more frequent and/or more persistent outbreaks of northerly and westerly cold air masses to the western Mediterranean, channelled through the Rhone valley and the northern Pyrenees rim, and entering the basin at the Gulf of Lyon (Cacho et al., 2001). Here, they caused higher wind stress, SST cooling and mixing of the water column (Cortina et al, 2011, 2013, 2015; Kuhlemann et al., 2008). Modern observations show that these cold-air outbreaks induce the rapid formation of a shallow vortex over the Gulf of Genoa, and stimulate cyclogenesis and moisture transport to the SW lee of the Alps (Aebischer and Schär, 1998). Interestingly, for the early MIS 6 (180−160 ka), the record from marine core PRLG 1, located in the Gulf of Lyon, shows a different pattern and generally cooler SSTs compared to other Mediterranean and mid-latitudes core locations, although local SSTs were higher than the ensuing and preceding intervals (Fig. 7). We suggest that during the 180−170 ka period, the interaction between the intensified north-westerly cold flow (relating to increased ice volume), and the relatively warm waters of the NW Mediterranean (due to the peculiar atmospheric configuration occurring at the precession minimum) strongly enhanced cyclogenesis in the Northern Tyrrhenian Sea. This fuelled intense precipitation to reach the Southern Alps, especially the SW sector where Rio Martino is located. At the same time, the warmer summer maintained high levels of ablation, promoting glacial retreat and vegetation development. After 170 ka, during the descending limb of precession, the decreased seasonal contrast caused a reduction in SST and weakened Mediterranean

cyclogenesis. This promoted the progressive reduction in precipitation evident in the RMD7 proxies. However, the persistence of cold outbreaks stimulating local atmospheric perturbations in the Northern Tyrrhenian Sea would have maintained elevated moisture transport towards the southern flank of the Alps, favouring snow accumulation in the glaciological catchment of the large piedmont glaciers. At the same time, the decrease in summer insolation led to reduced ablation. Glaciers were thus able to advance, although the overall arcuate E−W orientation of the southern Alpine fringe with respect to atmospheric circulation patterns may have led to extreme differences in precipitation rates across the Alps, and thus in glacier equilibrium lines altitudes (Ivy-Ochs, 2015; Luetscher et al., 2015; Florineth and Schluchter, 2000). This would have led to the end of the interstadial phase, almost coincident with the insolation minimum at ca. 160 ka (Fig. 7).

5.5. Millennial scale variability over the early MIS 6

Superimposed on the orbital-scale changes, the Rio Martino record shows prominent and rather periodic hydrological climate instability at sub-orbital scale, which shows a higher frequency in the phase of growth up to 170 ka, with five wetter/drier oscillations alternating with a rather regular period of ca. 2 kyr (Fig. 4). The large chronological uncertainty (average 2.8 kyr) associated with our record prevents a detailed discussion on the timing of this variability, and hampers our ability to correlate it with widespread evidence of multiple climate cycles within the early MIS 6 from Mediterranean and European lakes and speleothem records (Wainer et al., 2013; Roucoux et al., 2011; Plagnes et al., 2002). However, some consideration of its general structure, significance and forcing can be achieved by comparing it with hemispheric and global reference records available for this period. In the combined terrestrial and marine record from the Iberian Margin marine core MD01-2444 (Fig. 1), three marine-terrestrial interstadials are recognized in the 180−170 ka period (Fig. 8; Margari et al., 2014; 2010). They show coherent changes in surface and deep-water hydrography, consistent with the operation of the bipolar-seesaw, and a synchronous response of vegetation to millennial-scale changes in North Atlantic oceanic conditions. A tripartite structure is present also in the record of East Asian Monsoon intensity from Sanbao Cave speleothem in central China, where it is linked to a synchronous response of low-latitude circulation patterns to changes in North Atlantic heat content due to the bipolar seesaw (Fig. 8; Wang et al., 2008). Finally, the same pattern is apparent in the methane record from the EPICA Dome C (EDC) Antarctic ice core (Loulergue et al., 2008, Fig. 8), which can be used as a proxy of Northern Hemisphere millennial temperature fluctuations beyond the Greenland ice record (Masson-Delmotte et al., 2004). Within the combined age uncertainties, the millennial-scale structure of the RMD7 record shows an overall similarity with these records (Fig. 8). This suggests that over this period the hydrology of the Southern Alps responded coherently with hemispheric changes in climate, driven by perturbations of North Atlantic conditions, which were likely transmitted within the Mediterranean by changes in the strength and trajectory of westerlies (e.g. Margari et al., 2014). Interestingly, lithological, organic and paleo-productivity proxies from the S6 layers in Eastern Mediterranean cores also show high-frequency changes superimposed on the general insolation pattern, indicating unstable water column stratification (Rohling et al., 2015; Triantaphyllou et al., 2010; Schmiedl et al., 2003; Weldeab et al., 2003). These instabilities were linked to the influence of climatic boundary conditions in the northern catchment, and particularly to minor SST fluctuations at the millennial scale, possibly induced by northerly cold outbursts and high wind stress. In fact, the PRLG-1 record from the Gulf of
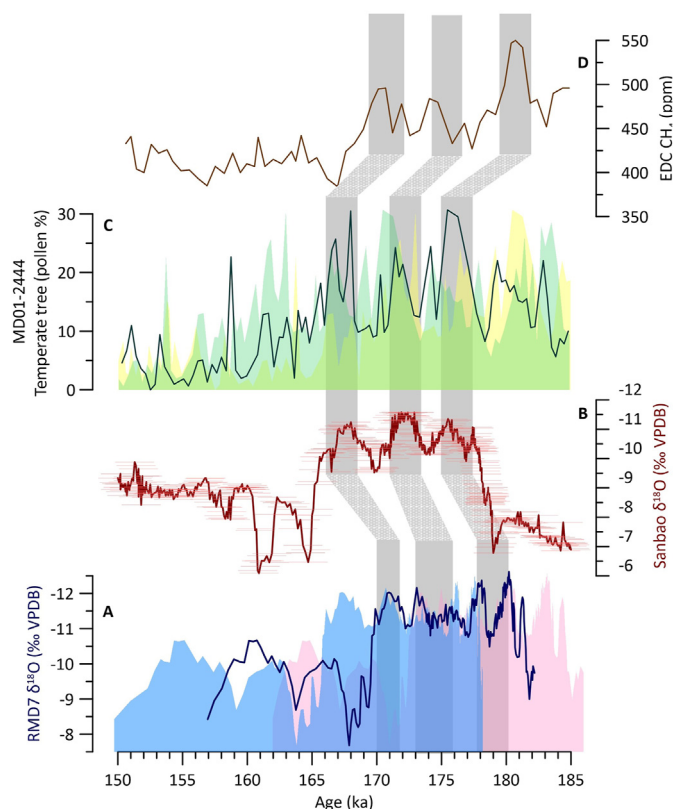
Fig. 8. A) RMD7 $\delta^{18}O$ (this study, the blue line is the central age, pink and light-blue shadings represent the associated negative and positive age uncertainties respectively); B) speleothem δ18O from Sanbao Cave with the related age uncertainty (Wang et al., 2008); C) Temperate tree pollen record from core MD01-2444, light-green and yellow shadings represent the associated negative and positive age uncertainties respectively); D) Methane record from Epica Dome C Antarctic core, reported on the AICC2012 chronology (Bazin et al., 2013). The grey rectangles indicates the three main interstadials during the early MIS 6. (For interpretation of the references to colour in this figure legend, the reader is referred to the Web version of this article.)

Lyon shows alternating intervals of higher/lower bottom water ventilation, related to stronger/weaker north-westerly flow and typically associated with cooling/warming of surface waters (Cortina et al., 2013, Fig. 7). Although the diverse resolution and poor chronological control of the marine records prevent detailed correlation with Rio Martino, we suggest that the related perturbations in local atmospheric circulation contributed to the short-term precipitation variability, modulating the hemispheric background variability related to North Atlantic oceanic conditions.

6. Conclusion

We have presented here a multiproxy speleothem record from Rio Martino Cave (SW Alps) covering the early part of MIS 6 (182−157 ka). The period of deposition, and particularly the 180−170 ka interval, corresponds to a wet interstadial phase that can be traced across the Southern Alps, and is characterized by glacial retreat and by the development of soils and vegetation up to 1900−2000 m a.s.l.. The wettest Alpine phase closely follows the pattern of precession, and corresponds to an interval of increased precipitation in the western Mediterranean and to the period of deposition of Sapropel S6 in the eastern Mediterranean. In the western Mediterranean, the atmospheric configuration related to sapropel formation led to warmer and drier summers and to increased local cyclogenesis and enhanced autumn precipitation (Wagner et al., 2019). The coherence observed between Rio Martino

and the Mediterranean records suggests that the effect of enhanced local cyclogenesis for the S6 interval was not restricted to the Mediterranean, but also reached the Southern Alps, contrasting with the Holocene Sapropel S1 (Spötl et al., 2010). We suggest that this is due to different boundary conditions during MIS6, particularly the interaction between the relatively warm waters of the NW Mediterranean, related to the insolation maximum, and the enhanced cold north westerly flow entering the basin at the Gulf of Lyon, related to increased ice volume in the northern North Atlantic during the glacial interval. This peculiar configuration likely stimulated autumn cyclogenesis in the Northern Tyrrhenian Sea, and caused intense moisture transport towards the Alps. Over this interval, glacial growth was likely inhibited by the high summer insolation, which enhanced summer melting. After 170 ka, in the descending limb of precession, the seasonal contrast weakened and summer temperatures decreased. This caused a progressive reduction in precipitation, but at the same time reduced summer ablation, favouring snow accumulation and glacier expansion, leading to the end of the interstadial at ca. 160 ka. Superimposed on the orbital pattern, the Rio Martino record shows prominent and episodic hydrologic instability at the millennial scale, particularly during the 180−170 ka period. The general pattern of this sub-orbital variability resembles hemispheric climate changes, and can be ultimately linked to the operation of the glacial bipolar seesaw.

Appendix A. Supplementary data

Supplementary data to this article can be found online at https://doi.org/10.1016/j.quascirev.2021.106856.

References

Aebischer, U., Schär, C., 1998. Low-level potential vorticity and cyclogenesis to the lee of the Alps. J. Atmos. Sci. 55 (2), 186−207.
Almqvist, B.S., Herwegh, M., Schmidt, V., Pettke, T., Hirt, A.M., 2010. Magnetic

susceptibility as a tool to study deformed calcite with variable impurity content. G-cubed 11 (1).

Ayalon, A., Bar-Matthews, M., Kaufman, A., 1999. Petrography, strontium, barium and uranium concentrations, and strontium and uranium isotope ratios in speleothems as palaeoclimatic proxies: Soreq Cave, Israel. Holocene 9 (6), 715–722.

Ayalon, A., Bar-Matthews, M., Kaufman, A., 2002. Climatic conditions during marine oxygen isotope stage 6 in the eastern Mediterranean region from the isotopic composition of speleothems of Soreq Cave, Israel. Geology 30 (4), 303–306.

Bajo, P., Drysdale, R.N., Woodhead, J.D., Hellstrom, J.C., Hodell, D., Ferretti, P., Voeler, A.h.L., Zanchetta, G., Rodrigues, T., Wolff, E., Tyler, J., Frisia, S., Spötl, C., Fallick, A.E., Tyler, J., 2020. Persistent influence of obliquity on ice age terminations since the Middle Pleistocene transition. Science 367 (6483), 1235–1239.

Bajo, P., Borsato, A., Drysdale, R., Hua, Q., Frisia, S., Zanchetta, G., Hellstrom, J.C., Woodhead, J., 2017. Stalagmite carbon isotopes and dead carbon proportion (DCP) in a near-closed-system situation: an interplay between sulphuric and carbonic acid dissolution. Geochem. Cosmochim. Acta 210, 208–227.

Baker, A., Hartmann, A., Duan, W., Hankin, S., Comas-Bru, L., Cuthbert, M.O., Treble, P.C., Banner, J., Genty, D., Baldini, L.M., Bartolomé, M., Moreno, A., Mejias, C.P., Werner, M., 2019. Global analysis reveals climatic controls on the oxygen isotope composition of cave drip water. Nat. Commun. 10 (1), 1–7.

Bard, E., Delaygue, G., Rostek, F., Antonioli, F., Silenzi, S., Schrag, D.P., 2002. Hydrological conditions over the western Mediterranean basin during the deposition of the cold Sapropel 6 (ca. 175 kyr BP). Earth Planet Sci. Lett. 202 (2), 481–494.

Bar-Matthews, M., Ayalon, A., Gilmour, M., Matthews, A., Hawkesworth, C.J., 2003. Sea–land oxygen isotopic relationships from planktonic foraminifera and speleothems in the Eastern Mediterranean region and their implication for paleorainfall during interglacial intervals. Geochem. Cosmochim. Acta 67 (17), 3181–3199.

Bazin, L., Landais, A., Lemieux-Dudon, B., Kele, H.T.M., Veres, D., Parrenin, F., Loutre, M.F., 2013. An Optimized Multi-Proxy, Multi-Site Antarctic Ice and Gas Orbital Chronology (AICC2012): 120-800 Ka.

Belli, R., Frisia, S., Borsato, A., Drysdale, R., Hellstrom, J., Zhao, J.X., Spötl, C., 2013. Regional climate variability and ecosystem responses to the last deglaciation in the northern hemisphere from stable isotope data and calcite fabrics in two northern Adriatic stalagmites. Quat. Sci. Rev. 72, 146–158.

Borradaile, G.J., Henry, B., 1997. Tectonic applications of magnetic susceptibility and its anisotropy. Earth Sci. Rev. 42 (1–2), 49–93.

Borsato, A., Frisia, S., Miorandi, R., 2015. Carbon dioxide concentration in temperate climate caves and parent soils over an altitudinal gradient and its influence on speleothem growth and fabrics. Earth Surf. Process. Landforms 40 (9), 1158–1170.

Bosmans, J.H.C., Drijfhout, S.S., Tuenter, E., Hilgen, F.J., Lourens, L.J., Rohling, E.J., 2015. Precession and obliquity forcing of the freshwater budget over the Mediterranean. Quat. Sci. Rev. 123, 16–30.

Bourne, M.D., Feinberg, J.M., Strauss, B.E., Hardt, B., Cheng, H., Rowe, H.D., Springer, G., Edwards, R.L., 2015. Long-term changes in precipitation recorded by magnetic minerals in speleothems. Geology 43 (7), 595–598.

Boyd, E.S., Hamilton, T.L., Havig, J.R., Skidmore, M.L., Shock, E.L., 2014. Chemolithotrophic primary production in a subglacial ecosystem. Appl. Environ. Microbiol. 80 (19), 6146–6153.

Cacho, I., Grimalt, J.O., Canals, M., Sbaffi, L., Shackleton, N.J., Schönfeld, J., Zahn, R., 2001. Variability of the western Mediterranean Sea surface temperature during the last 25,000 years and its connection with the Northern Hemisphere climatic changes. Paleoceanography 16 (1), 40–52.

Casty, C., Wanner, H., Luterbacher, J., Esper, J., Böhm, R., 2005. Temperature and precipitation variability in the European Alps since 1500. Int. J. Climatol.: A Journal of the Royal Meteorological Society 25 (14), 1855–1880.

Cerling, T.E., Solomon, D.K., Quade, J.A.Y., Bowman, J.R., 1991. On the isotopic composition of carbon in soil carbon dioxide. Geochem. Cosmochim. Acta 55 (11), 3403–3405.

Cerling, T.E., Wang, Y., Quade, J., 1993. Expansion of C4 ecosystems as an indicator of global ecological change in the late Miocene. Nature 361 (6410), 344–345.

Cheng, H., Edwards, R.L., Sinha, A., Spötl, C., Yi, L., Chen, S., Lelly, M., Kathayat, G., Wang, X., Kong, X., Wang, Y., Ning, Y., Zhang, H., 2016. The Asian monsoon over the past 640,000 years and ice age terminations. Nature 534 (7609), 640–646.

Columbu, A., Drysdale, R., Capron, E., Woodhead, J., De Waele, J., Sanna, L., Hellstrom, J.C., Bajo, P., 2017. Early last glacial intra-interstadial climate variability recorded in a Sardinian speleothem. Quat. Sci. Rev. 169, 391–397.

Columbu, A., Sauro, F., Lundberg, J., Drysdale, R., De Waele, J., 2018. Palaeoenvironmental changes recorded by speleothems of the southern Alps (Piani Eterni, Belluno, Italy) during four interglacial to glacial climate transitions. Quat. Sci. Rev. 197, 319–335.

Cortina, A., Sierro, F.J., Flores, J.A., Martrat, B., Grimalt, J.O., 2015. The response of SST to insolation and ice sheet variability from MIS 3 to MIS 11 in the northwestern Mediterranean Sea (Gulf of Lions). Geophys. Res. Lett. 42 (23), 10–366.

Cortina, A., Sierro, F.J., Filippelli, G., Flores, J.A., Berné, S., 2013. Changes in planktic and benthic foraminifer assemblages in the Gulf of Lions, off south France: response to climate and sea level change from MIS 6 to MIS 11. G-cubed 14 (4), 1258–1276.

Cortina, A., Sierro, F.J., González-Mora, B., Asioli, A., Flores, J.A., 2011. Impact of climate and sea level changes on the ventilation of intermediate water and benthic foraminifer assemblages in the Gulf of Lions, off South France, during MIS 6 and 7. Palaeogeogr. Palaeoclimatol. Palaeoecol. 309 (3–4), 215–228.

Daëron, M., Drysdale, R.N., Peral, M., Huyghe, D., Blamart, D., Coplen, T.B., Lartaud, F., Zanchetta, G., 2019. Most Earth-surface calcites precipitate out of isotopic equilibrium. Nat. Commun. 10 (1), 1–7.

Dehnert, A., Preusser, F., Kramers, J.D., Akçar, N., Kubik, P.W., Reber, R., Schlüchter, C., 2010. A multi-dating approach applied to proglacial sediments attributed to the most extensive Glaciation of the Swiss Alps. Boreas 39, 620–632.

Dehnert, A., Lowick, S.E., Preusser, F., Anselmetti, F.S., Drescher-Schneider, R., Graf, H.R., Heller, F., Horstmeyer, H., Kemna, H.A., Nowaczyk, N.R., Züger, A., Furrer, H., 2012. Evolution of an overdeepened trough in the northern alpine foreland at Niederweningen, Switzerland. Quat. Sci. Rev. 34, 127–145.

Demény, A., Németh, P., Czuppon, G., Leél-Össy, S., Szabó, M., Judik, K., Stieber, J., 2016. Formation of amorphous calcium carbonate in caves and its implications for speleothem research. Sci. Rep. 6, 39602.

Drysdale, R.N., Zanchetta, G., Hellstrom, J.C., Fallick, A.E., Zhao, J.X., 2005. Stalagmite evidence for the onset of the Last Interglacial in southern Europe at 129 ± 1 ka. Geophys. Res. Lett. 32 (24).

Efthymiadis, D., Jones, P.D., Briffa, K.R., Böhm, R., Maugeri, M., 2007. Influence of large-scale atmospheric circulation on climate variability in the Greater Alpine Region of Europe. J. Geophys. Res.: Atmospheres 112 (D12).

Ehleringer, J.R., Buchmann, N., Flanagan, L.B., 2000. Carbon isotope ratios in belowground carbon cycle processes. Ecol. Appl. 10 (2), 412–422.

Fairchild, I.J., Treble, P.C., 2009. Trace elements in speleothems as recorders of environmental change. Quat. Sci. Rev. 28 (5–6), 449–468.

Federici, P.R., Ribolini, A., Spagnolo, M., 2017. Glacial history of the Maritime Alps from the last glacial maximum to the little ice age. Geological Society, London, Special Publications 433 (1), 137–159.

Finné, M., Bar-Matthews, M., Holmgren, K., Sundqvist, H.S., Liakopoulos, I., Zhang, Q., 2014. Speleothem evidence for late Holocene climate variability and floods in Southern Greece. Quaternary Research 81 (2), 213–227.

Florineth, D., Schlüchter, C., 2000. Alpine evidence for atmospheric circulation patterns in Europe during the last glacial maximum. Quaternary Research 54 (3), 295–308.

Francke, A., Wagner, B., Just, J., Leicher, N., Gromig, R., Baumgarten, H., Leng, M.J., 2016. Sedimentological processes and environmental variability at Lake Ohrid (Macedonia, Albania) between 637 ka and the present. Biogeosciences 13 (4), 1179–1196.

Frei, C., Schär, C., 1998. A precipitation climatology of the Alps from high-resolution rain-gauge observations. Int. J. Climatol.: A Journal of the Royal Meteorological Society 18 (8), 873–900.

Frisia, S., Borsato, A., Hellstrom, J., 2018. High spatial resolution investigation of nucleation, growth and early diagenesis in speleothems as exemplar for sedimentary carbonates. Earth Sci. Rev. 178, 68–91.

Frisia, S., Weyrich, L.S., Hellstrom, J., Borsato, A., Golledge, N.R., Anesio, A.M., Cooper, A., 2017. The influence of Antarctic subglacial volcanism on the global iron cycle during the Last Glacial Maximum. Nat. Commun. 8 (1), 1–9.

Frisia, S., 2015. Microstratigraphic logging of calcite fabrics in speleothems as tool for palaeoclimate studies. Int. J. Speleol. 44 (1), 1.

Frisia, S., Borsato, A., 2010. Karst. Dev. Sedimentol. 61, 269–318.

Frumkin, A., Stein, M., 2004. The Sahara–East Mediterranean dust and climate connection revealed by strontium and uranium isotopes in a Jerusalem speleothem. Earth Planet Sci. Lett. 217 (3–4), 451–464.

Genty, D., Blamart, D., Ouahdi, R., Gilmour, M., Baker, A., Jouzel, J., Van-Exter, S., 2001. Precise dating of Dansgaard–Oeschger climate oscillations in western Europe from stalagmite data. Nature 421, 833–837.

Giustini, F., Brilli, M., Patera, A., 2016. Mapping oxygen stable isotopes of precipitation in Italy. J. Hydrol.: Reg. Stud. 8, 162–181.

Gobiet, A., Kotlarski, S., Beniston, M., Heinrich, G., Rajczak, J., Stoffel, M., 2014. 21st century climate change in the European Alps—a review. Sci. Total Environ. 493, 1138–1151.

Graf, A.A., Strasky, S., Ivy-Ochs, S., Akçar, N., Kubik, P.W., Burkhard, M., Schlüchter, C., 2007. First results of cosmogenic dated pre-Last Glaciation erratics from the Montoz area, Jura Mountains, Switzerland. Quat. Int. 164, 43–52.

Häuselmann, A.D., Fleitmann, D., Cheng, H., Tabersky, D., Günther, D., Edwards, R.L., 2015. Timing and nature of the penultimate deglaciation in a high alpine stalagmite from Switzerland. Quat. Sci. Rev. 126, 264–275.

Hellstrom, J.C., McCulloch, M.T., 2000. Multi-proxy constraints on the climatic significance of trace element records from a New Zealand speleothem. Earth Planet Sci. Lett. 179 (2), 287–297.

Hellstrom, J., 2003. Rapid and accurate U/Th dating using parallel ion-counting multi-collector ICP-MS. Journal of Analytical Atomic Spectrometry 18 (11), 1346–1351.

Hellstrom, J., 2006. U–Th dating of speleothems with high initial 230Th using stratigraphical constraint. Quat. Geochronol. 1 (4), 289–295.

Hendy, C.H., 1971. The calculation of the effects of different modes of formation on the isotopic composition of speleothems and their applicability as palaeoclimatic indicators. Geochem. Cosmochim. Acta 35, 801–824.

Hercman, H., Gąsiorowski, M., Pawlak, J., Błaszczyk, M., Gradziński, M., Matoušková, Š., et al., 2020.). Atmospheric Circulation and the Differentiation of Precipitation Sources during the Holocene Inferred from Five Stalagmite Records from Demänová Cave System (Central Europe. The Holocene, 0959683620902224.

Holzkämper, S., Spötl, C., Mangini, A., 2005. High-precision constraints on timing of Alpine warm periods during the middle to late Pleistocene using speleothem growth periods. Earth Planet Sci. Lett. 236 (3–4), 751–764.

IPCC, 2019. Special Special Report on the Ocean and Cryosphere in a Changing

Climate: High Mountain Areas. https://www.ipcc.ch/srocc/.

Isola, I., Ribolini, A., Zanchetta, G., Bini, M., Regattieri, E., Drysdale, R.N., Hellstrom, J.C., Bajo, P., Montagna, P., Pons-Branchu, E., 2019. Speleothem U/Th age constraints for the last glacial conditions in the Apuan Alps, northwestern Italy. Palaeogeogr. Palaeoclimatol. Palaeoecol. 518, 62–71.

Ivy-Ochs, S., 2015. Glacier variations in the European Alps at the end of the last glaciation. Cuadernos de investigación geográfica/Geographical Research Letters 41, 295–315.

Kaufman, A., Wasserburg, G.J., Porcelli, D., Bar-Matthews, M., Ayalon, A., Halicz, L., 1998. U-Th isotope systematics from the Soreq cave, Israel and climatic correlations. Earth Planet Sci. Lett. 156 (3–4), 141–155.

Kim, S.T., O'Neil, J.R., 1997. Equilibrium and nonequilibrium oxygen isotope effects in synthetic carbonates. Geochem. Cosmochim. Acta 61 (16), 3461–3475.

Kuhlemann, J., Rohling, E.J., Krumrei, I., Kubik, P., Ivy-Ochs, S., Kucera, M., 2008. Regional synthesis of Mediterranean atmospheric circulation during the last glacial maximum. Science 321 (5894), 1338–1340.

Lachniet, M.S., 2009. Climatic and environmental controls on speleothem oxygen-isotope values. Quat. Sci. Rev. 28 (5–6), 412–432.

Lisiecki, L.E., Raymo, M.E., 2005. A Pliocene-Pleistocene stack of 57 globally distributed benthic δ18O records. Paleoceanography 20 (1).

López-Moreno, J.I., Vicente-Serrano, S.M., Morán-Tejeda, E., Lorenzo-Lacruz, J., Kenawy, A., Beniston, M., 2011. Effects of the North Atlantic Oscillation (NAO) on combined temperature and precipitation winter modes in the Mediterranean mountains: observed relationships and projections for the 21st century. Global Planet. Change 77 (1–2), 62–76.

Loulergue, L., Schilt, A., Spahni, R., Masson-Delmotte, V., Blunier, T., Lemieux, B., et al., 2008. Orbital and millennial-scale features of atmospheric CH 4 over the past 800,000 years. Nature 453 (7193), 383–386.

Luetscher, M., Hoffmann, D.L., Frisia, S., Spötl, C., 2011. Holocene glacier history from alpine speleothems, Milchbach cave, Switzerland. Earth Planet Sci. Lett. 302 (1–2), 95–106.

Luetscher, M., Boch, R., Sodemann, H., Spötl, C., Cheng, H., Edwards, R.L., Frisia, S., Hof, F., Müller, W., 2015. North Atlantic storm track changes during the last glacial maximum recorded by alpine speleothems. Nat. Commun. 6 (1), 1–6.

Magrì, F., Associazione Gruppi Speleologici Piemontesi (AGSP), 2007. La Grotta di Rio Martino (Valle Po-Piemonte). In: Magrì, F. (Ed.). Pubs. Regione Piemonte, pp. 5–98.

Maher, B.A., Alekseev, A., Alekseeva, T., 2003. Magnetic mineralogy of soils across the Russian Steppe: climatic dependence of pedogenic magnetite formation. Palaeogeogr. Palaeoclimatol. Palaeoecol. 201 (3–4), 321–341.

Margari, V., Skinner, L.C., Tzedakis, P.C., Ganopolski, A., Vautravers, M., Shackleton, N.J., 2010. The nature of millennial-scale climate variability during the past two glacial periods. Nat. Geosci. 3 (2), 127–131.

Margari, V., Skinner, L.C., Hodell, D.A., Martrat, B., Toucanne, S., Grimalt, J.O., Gibbard, P.L., Lunkka, J.P., Tzedakis, P.C., 2014. Land-ocean changes on orbital and millennial time scales and the penultimate glaciation. Geology 42 (3), 183–186.

Marino, G., Rohling, E.J., Rodríguez-Sanz, L., Grant, K.M., Heslop, D., Roberts, A.P., Yu, J., 2015. Bipolar seesaw control on last interglacial sea level. Nature 522 (7555), 197–201.

Martrat, B., Grimalt, J.O., Shackleton, N.J., de Abreu, L., Hutterli, M.A., Stocker, T.F., 2007. Four climate cycles of recurring deep and surface water destabilizations on the Iberian margin. Science 317 (5837), 502–507.

Masson-Delmotte, V., Chappellaz, J., Brook, E., Yiou, P., Barnola, J.M., Goujon, C., Lipenkov, V.I., 2004. Atmospheric methane during the last four glacial-interglacial cycles: rapid changes and their link with Antarctic temperature. J. Geophys. Res.: Atmospheres 109 (D12).

Milner, A.M., Collier, R.E., Roucoux, K.H., Müller, U.C., Pross, J., Kalaitzidis, S., Tzedakis, P.C., 2012. Enhanced seasonality of precipitation in the Mediterranean during the early part of the Last Interglacial. Geology 40 (10), 919–922.

Nehme, C., Verheyden, S., Breitenbach, S.F., Gillikin, D.P., Verheyden, A., Cheng, H., et al., 2018. Climate dynamics during the penultimate glacial period recorded in a speleothem from Kanaan Cave, Lebanon (central Levant). Quaternary Research 90 (1), 10–25.

Paterson, W.S.B., 1994. Physics of Glaciers. Butterworth-Heinemann.

Pausata, F.S., Li, C., Wettstein, J., Kageyama, M., Nisancioglu, K.H., 2011. The Key Role of Topography in Altering North Atlantic Atmospheric Circulation during the Last Glacial Period. Past climate variability: model analysis and proxy intercomparison.

Pini, R., Ravazzi, C., Donegana, M., 2009. Pollen stratigraphy, vegetation and climate history of the last 215 ka in the Azzano Decimo core (plain of Friuli, northeastern Italy). Quat. Sci. Rev. 28 (13–14), 1268–1290.

Plagnes, V., Causse, C., Genty, D., Paterne, M., Blamart, D., 2002. A discontinuous climatic record from 187 to 74 ka from a speleothem of the Clamouse Cave (south of France). Earth Planet Sci. Lett. 201 (1), 87–103.

Refsnider, K.A., Miller, G.H., Fogel, M.L., Fréchette, B., Bowden, R., Andrews, J.T., Farmer, G.L., 2014. Subglacially precipitated Carbonates record geochemical interactions and pollen preservation at the base of the Laurentide Ice Sheet on central Baffin Island, eastern Canadian Arctic. Quaternary research 81 (1), 94–105.

Regattieri, E., Zanchetta, G., Drysdale, R.N., Isola, I., Hellstrom, J.C., Roncioni, A., 2014. A continuous stable isotope record from the penultimate glacial maximum to the Last Interglacial (159–121 ka) from Tana Che Urla Cave (Apuan Alps, central Italy). Quaternary Research 82 (2), 450–461.

Regattieri, E., Giaccio, B., Zanchetta, G., Drysdale, R.N., Galli, P., Nomade, S.,

Peronace, E., Wulf, S., 2015. Hydrological variability over the Apennines during the Early Last Glacial precession minimum, as revealed by a stable isotope record from Sulmona basin, Central Italy. J. Quat. Sci. 30 (1), 19–31.

Regattieri, E., Zanchetta, G., Isola, I., Bajo, P., Perchiazzi, N., Drysdale, R.N., Boschi, C., Hellstrom, J.C., Francke, A., Wagner, B., 2018. A MIS 9/MIS 8 speleothem record of hydrological variability from Macedonia (FYROM). Global Planet. Change 162, 39–52.

Regattieri, E., Zanchetta, G., Isola, I., Zanella, E., Drysdale, R.N., Hellstrom, J.C., Zerboni, A., Dallai, L., Tema, E., Lanci, L., Costa, E., 2019a. Holocene Critical Zone dynamics in an Alpine catchment inferred from a speleothem multiproxy record: disentangling climate and human influences. Sci. Rep. 9 (1), 1–13.

Regattieri, E., Isola, I., Zanchetta, G., Tognarelli, A., Hellstrom, J.C., Drysdale, R.N., Boschi, C., Milevski, I., Temovski, M., 2019b. Middle-holocene climate variability from a stalagmite from Alilica cave (southern Balkans). Alpine and Mediterranean Quaternary 32 (1).

Riotte, J., Chabaux, F., Benedetti, M., Dia, A., Gérard, M., Boulègue, J., Etamé, J., 2003. Uranium colloidal transport and origin of the 234U–238U fractionation in surface waters: new insights from Mount Cameroon. Chem. Geol. 202 (3–4), 365–381.

Rohling, E.J., Marino, G., Grant, K.M., 2015. Mediterranean climate and oceanography, and the periodic development of anoxic events (sapropels). Earth Sci. Rev. 143, 62–97.

Romanek, C.S., Grossman, E.L., Morse, J.W., 1992. Carbon isotopic fractionation in synthetic aragonite and calcite: effects of temperature and precipitation rate. Geochem. Cosmochim. Acta 56, 419–430.

Roucoux, K.H., Tzedakis, P.C., Lawson, I.T., Margari, V., 2011. Vegetation history of the penultimate glacial period (Marine isotope stage 6) at Ioannina, north-west Greece. J. Quat. Sci. 26 (6), 616–626.

Rozanski, K., Araguás-Araguás, L., Gonfiantini, R., 1993. Isotopic patterns in modern global precipitation. Climate change in continental isotopic records 78, 1–36.

Rudzka, D., McDermott, F., Baldini, L.M., Fleitmann, D., Moreno, A., Stoll, H., 2011. The coupled δ13C-radiocarbon systematics of three Late Glacial/early Holocene speleothems; insights into soil and cave processes at climatic transitions. Geochem. Cosmochim. Acta 75 (15), 4321–4339.

Schmiedl, G., Mitschele, A., Beck, S., Emeis, K.C., Hemleben, C., Schulz, H., et al., 2003. Benthic foraminiferal record of ecosystem variability in the eastern Mediterranean Sea during times of sapropel S5 and S6 deposition. Palaeogeogr. Palaeoclimatol. Palaeoecol. 190, 139–164.

Spötl, C., Mangini, A., 2002. Stalagmite from the Austrian Alps reveals Dansgaard–Oeschger events during isotope stage 3: implications for the absolute chronology of Greenland ice cores. Earth Planet. Sc. Lett. 203 (1), 507–518.

Spötl, C., Mangini, A., Bums, S.J., Frank, N., Pavuza, R., 2004. Speleothems from the high-alpine Spannagel cave, Zillertal Alps (Austria). In: Studies of Cave Sediments. Springer, Boston, MA, pp. 243–256.

Spötl, C., Nicolussi, K., Patzelt, G., Boch, R., 2010. Humid climate during deposition of sapropel 1 in the Mediterranean Sea: Assessing the influence on the Alps. Global Planet. Change 71 (3–4), 242–248.

Sodemann, H., Zubler, E., 2010. Seasonal and inter-annual variability of the moisture sources for Alpine precipitation during 1995–2002. Int. J. Climatol.: A Journal of the Royal Meteorological Society 30 (7), 947–961.

Spötl, C., Mangini, A., 2007. Speleothems and paleoglaciers. Earth Planet Sci. Lett. 254 (3–4), 323–331.

Suklitsch, M., Gobiet, A., Truhetz, H., Awan, N.K., Göttel, H., Jacob, D., 2011. Error characteristics of high resolution regional climate models over the Alpine area. Clim. Dynam. 37 (1–2), 377–390.

Thomazo, C., Buoncristiani, J.F., Vennin, E., Pellenard, P., Cocquerez, T., Mugnier, J.L., Gérard, E., 2017. Geochemical processes leading to the precipitation of subglacial carbonate crusts at bossons glacier, mont blanc massif (French Alps). Front. Earth Sci. 5, 70.

Toucanne, S., Minto'o, C.M.A., Fontanier, C., Bassetti, M.A., Jorry, S.J., Jouet, G., 2015. Tracking rainfall in the northern Mediterranean borderlands during sapropel deposition. Quat. Sci. Rev. 129, 178–195.

Tremaine, D.M., Froelich, P.N., Wang, Y., 2011. Speleothem calcite farmed in situ: modern calibration of δ18O and δ13C paleoclimate proxies in a continuously-monitored natural cave system. Geochem. Cosmochim. Acta 75, 4929–4950.

Triantaphyllou, M.V., Antonarakou, A., Dimiza, M., Anagnostou, C., 2010. Calcareous nannofossil and planktonic foraminiferal distributional patterns during deposition of sapropels S6, S5 and S1 in the Libyan Sea (Eastern Mediterranean). Geo Mar. Lett. 30 (1), 1–13.

Tzedakis, P.C., 2007. Seven ambiguities in the Mediterranean palaeoenvironmental narrative. Quat. Sci. Rev. 26 (17–18), 2042–2066.

Tzedakis, P.C., Drysdale, R.N., Margari, V., Skinner, L.C., Menviel, L., Rhodes, R.H., Taschetto, A.S., Hodell, D., Crowhurst, S.J., Hellstrom, J.C., Fallick, A.E., Grimalt, J.O., McManus, J.F., Martrat, B., Mokkedem, Z., Parrenin, F., Regattieri, E., Roe, K., Zanchetta, G., 2018. Enhanced climate instability in the north Atlantic and southern Europe during the last interglacial. Nat. Commun. 9 (1), 1–14.

Vaks, A., Bar-Matthews, M., Ayalon, A., Matthews, A., Frumkin, A., Dayan, U., Schilman, B., 2006. Paleoclimate and location of the border between Mediterranean climate region and the Saharo–Arabian Desert as revealed by speleothems from the northern Negev Desert, Israel. Earth Planet Sci. Lett. 249 (3–4), 384–399.

Wainer, K., Genty, D., Blamart, D., Bar-Matthews, M., Quinif, Y., Plagnes, V., 2013. Millennial climatic instability during penultimate glacial period recorded in a south-western France speleothem. Palaeogeogr. Palaeoclimatol. Palaeoecol. 376,

122−131.

Wagner, B., Vogel, H., Francke, A., Friedrich, T., Donders, T., Lacey, J.H., Leng, M.J., Regattieri, E., Sadori, L., Wilke, T., Zanchetta, G., Albrecht, C., Bertini, A., Combourieu-Nebout, N., Cvetkoska, A., Giaccio, B., Grazhdani, A., Hauffe, T., Holtvoeth, J., Joannin, S., Jovanovska, E., Just, J., Kouli, K., Kousis, I., Koutsodendris, A., Krastel, S., Lagos, M., Leicher, N., Levkov, Z., Lindhorst, K., Masi, A., Melles, M., Mercuri, A.m., Nomade, S., Nowaczyk, n., Panagiotopoulos, K., Peyron, O., Reed, J.M., Sagnotti, L., Sinopoli, G., Stelbrink, B., Sulpizio, R., Timmermann, A., Tofilovska, S., Torri, P., Wagner-Cremer, F., Wonik, T., Zhange, X., 2019. Mediterranean winter rainfall in phase with African monsoons during the past 1.36 million years. Nature 573 (7773), 256−260.

Wang, Y., Cheng, H., Edwards, R.L., Kong, X., Shao, X., Chen, S., et al., 2008. Millennial-and orbital-scale changes in the East Asian monsoon over the past 224,000 years. Nature 451 (7182), 1090−1093.

Wanner, H., Rickli, R., Salvisberg, E., Schmutz, C., Schüepp, M., 1997. Global climate change and variability and its influence on alpine climate—concepts and observations. Theor. Appl. Climatol. 58 (3), 221−243.

Weldeab, S., Emeis, K.C., Hemleben, C., Schmiedl, G., Schulz, H., 2003. Spatial productivity variations during formation of sapropels S5 and S6 in the Mediterranean Sea: evidence from Ba contents. Palaeogeogr. Palaeoclimatol. Palaeoecol. 191 (2), 169−190.

Zanchetta, G., Drysdale, R.N., Hellstrom, J.C., Fallick, A.E., Isola, I., Gagan, M.K., Pareschi, M.T., 2007. Enhanced rainfall in the Western Mediterranean during deposition of sapropel S1: stalagmite evidence from Corchia cave (Central Italy). Quat. Sci. Rev. 26 (3−4), 279−286.

Zanella, E., Tema, E., Lanci, L., Regattieri, E., Isola, I., Hellstrom, J.C., Costa, E., Zanchetta, G., Drysdale, R.N., Magrì, F., 2018. A 10,000 yr record of high-resolution Paleosecular variation from a flowstone of Rio Martino cave, northwestern Alps, Italy. Earth Planet Sci. Lett. 485, 32−42.

Zhang, J., Quay, P.D., Wilbur, D.O., 1995. Carbon isotope fractionation during gas-water exchange and dissolution of CO2. Geochem. Cosmochim. Acta 59, 107−114.

Zhornyak, L.V., Zanchetta, G., Drysdale, R.N., Hellstrom, J.C., Isola, I., Regattieri, E., Piccini, L., Baneschi, I., Couchoud, I., 2011. Stratigraphic evidence for a "pluvial phase" between ca 8200−7100 ka from Renella cave (Central Italy). Quat. Sci. Rev. 30 (3−4), 409−417.

Ziegler, M., Tuenter, E., Lourens, L.J., 2010. The precession phase of the boreal summer monsoon as viewed from the eastern Mediterranean (ODP Site 968). Quat. Sci. Rev. 29 (11−12), 1481−1490.

Zhu, Z., Zhang, S., Tang, C., Li, H., Xie, S., Ji, J., Xiao, G., 2012. Magnetic fabric of stalagmites and its formation mechanism. G-cubed 13 (6).